arXiv:1411.5885v1 [nlin.PS] 21 Nov 2014

Fluxon mobility in an asymmetric SQUID array

Yaroslav Zolotaryuk* and Ivan O. Starodub†
Bogolyubov Institute for Theoretical Physics, National Academy of Sciences of Ukraine, vul. Metrologichna 14B, 03680 Kyiv, Ukraine
(Dated: November 24, 2014)

Fluxon dynamics in the dc-biased array of asymmetric three-junction superconducting quantum interference devices (SQUIDs) is investigated. The array of SQUIDs is described by the discrete double sine-Gordon equation. It appears that this equation possesses a finite set of velocities at which the fluxon propagates with the constant shape and without radiation. The signatures of these velocities appear on the respective current-voltage characteristics of the array as inaccessible voltage intervals (gaps). The critical depinning current has a clear minimum as a function of the asymmetry parameter (the ratio of the critical currents of the left and right junctions of the SQUID), which coincides with the minimum of the Peierls-Nabarro potential.

PACS numbers: 05.45.Yv, 63.20.Ry, 05.45.-a, 03.75.Lm

I. INTRODUCTION

Arrays of Josephson devices have been studied intensively during the last several decades [1, 2]. The recent interest to these objects has been stimulated by the applications in quantum computing [3, 4] or design of metamaterials, based on the arrays of rf-biased SQUIDs (superconducting quantum interference devices) [5]. The effect of relativistic time dilation has been suggested in the array of asymmetric SQUIDs [6]. This system is described by the double discrete sine-Gordon (DDbSG) equation [6] and it will be the subject of the current article.

On the other hand, the problem of topological soliton (kink or antikink) mobility in discrete media has attracted much attention within recent years. It has been demonstrated that solitary waves in nonlinear lattices can propagate with constant shape and velocity without any radiation [7–16] despite the presence of the non-zero Peierls-Nabarro potential. These solutions are spatially localized (have finite energy) and exist for a discrete set of velocities, in contrast to the continuous models where the allowed velocities usually occupy a continuous interval, bound from the above by some critical velocity value. Since their existence is associated with avoiding the resonances with the linear spectrum of the underlying system, they are called *embedded* solitons [17]. These solitons exist in different systems, including the continuum versions of the sine-Gordon [18] and double sine-Gordon [19] equations with the high-order dispersion. In this article it will be shown that the DDbSG equation, that models the asymmetric SQUID array, also possesses discrete embedded solitons. Taking into account that the model of the SQUID array is based on the RCJM (resistively and capacitively shunted junction model), the consideration of dissipation and external dc bias is essential, and this also will be done in the current article.

*Electronic address: yzolo@bitp.kiev.ua
†Electronic address: starodub@bitp.kiev.ua

Thus, the aim of this work is twofold: (i) to study the dynamical fluxon properties in the SQUID array, and, in particular, to obtain the current-voltage characteristics (CVCs) of the array; (ii) to demonstrate the signatures of the fluxon as an embedded soliton that moves along the array without significant radiation.

The paper is organized as follows. The model of the asymmetric SQUID array is described in the next section. In Sec. III we discuss the properties of the DDbSG lattice in the Hamiltonian limit. Next section is devoted to the current-voltage characteristics. Discussion and conclusions are given in the last section.

II. THE MODEL

In this paper, we discuss the dynamics of the dc-biased array of asymmetric three-junction SQUIDs. Each elementary cell of the array is the SQUID that consists of three Josephson junctions, two identical junctions are placed in the left arm and one of them is placed in the right arm, as shown schematically in Fig. 1 (a more detailed equivalent scheme is given in Fig. 1 of Ref. [6]). In the nth SQUID $\phi_n^{(l)}/2$ is the Josephson phase of one of the left junctions and $\phi_n^{(r)}$ is the Josephson phase of the right junction. The whole system is described by the dc-driven and damped DDbSG equation, which can be written in the dimensionless form as follows

$$\ddot{\phi}_n - \kappa\,\hat{\Delta}\phi_n + \frac{2}{1+2\eta}\left(\eta\sin\phi_n + \sin\frac{\phi_n}{2}\right) + \alpha\dot{\phi}_n = \gamma, \quad n = 1, 2, \ldots, N\,. \tag{1}$$

The derivation of this equation from the Kirchhoff laws and the Josephson equations has been performed previously [6]. Under the assumption of the small loop size the single phase difference $\phi_n = \phi_n^{(l)} = \phi_n^{(r)}$ has been introduced and $\hat{\Delta}\phi_n \doteq \phi_{n+1} - 2\phi_n + \phi_{n-1}$ is the discrete Laplacian. In this model only the self-inductance is taken into account, while the mutual inductances of the SQUIDs are neglected, in accordance with the previous

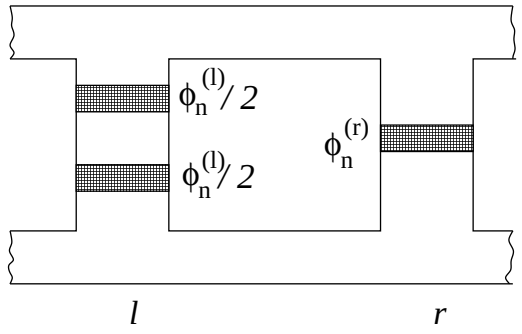

FIG. 1: Schematic view of the elementary cell of the SQUID array. The detailed equivalent scheme is given by Fig. 1 of Ref. [6]. Also see text for details.

work [20]. Other dimensionless parameters are defined as follows

$$\alpha = \frac{1}{RC\omega_J}, \quad \kappa = \frac{\Phi_0}{2\pi L I_c}, \quad \eta = \frac{I_c^{(r)}}{I_c^{(l)}} , \tag{2}$$
$$C = C_l + \frac{C_r}{2}, \quad \frac{1}{R} = \frac{1}{R_r} + \frac{1}{2R_l}, \quad I_c = I_c^{(r)} + \frac{I_c^{(l)}}{2} .$$

Here $\omega_J = \sqrt{2eI_c/(C\hbar)}$ is the Josephson plasma frequency and the dimensionless time in Eq. (1) is normalized in the units of ω_J^{-1}, α is the dissipation parameter, Φ_0 is the magnetic flux quantum, L is the elementary cell inductance and γ is the dimensionless external bias current, normalized to I_c. Next, $R_{r,l}$, $C_{r,l}$ and $I_c^{(r,l)}$ are, respectively, the resistance, capacitance and critical current of the right or the left junction (marked by the sub(super)script "r" or "l"). The parameter η measures the asymmetry of the SQUID and is the ratio of the critical currents of the right and left junctions of the SQUID.

Two limits of Eq. (1) are important. If $\eta = 0$, one obtains the discrete sine-Gordon (DSG) equation with the term $\sin(\phi_n/2)$, while if $\eta \to \infty$ the DSG equation is restored, but with the $\sin\phi_n$ term. The former case physically means that the $I_c^{(r)} \to \infty$, thus the left arm of the SQUID effectively disappears. The latter case means that $I_c^{(l)} \to \infty$ and the same happens to the right arm. In both the cases the elementary cell of the array becomes symmetric.

The circular array is to be considered, thus, the boundary conditions read $\phi_n = \phi_{n+N} + 4\pi Q$, where Q is the total topological charge, i.e., the total number of fluxons and anti-fluxons trapped in the ring. In this article only the case of one fluxon in the array will be considered, hence $Q = 1$.

III. THE HAMILTONIAN LIMIT

The fluxon dynamics in the real SQUID array can be understood better if the Hamiltonian limit $\alpha = \gamma = 0$ is considered first. As a result, Eq. (1) can be considered as the equation of motion of the lattice that is governed by the Hamiltonian function

$$H = \sum_{n=1}^{N} \left[\frac{\dot{\phi}_n^2}{2} + \frac{\kappa}{2}(\phi_{n+1} - \phi_n)^2 + V(\phi_n) \right], \tag{3}$$

where the on-site potential $V(\phi)$ is expressed as

$$V(\phi) = V_0 \left[\eta(1 - \cos\phi) + 2\left(1 - \cos\frac{\phi}{2}\right) \right],$$
$$V_0 = \frac{2}{1 + 2\eta} . \tag{4}$$

The variable ϕ_n can be treated as the coordinate of the respective particle of the lattice. The shape of the potential (4) is depicted in Fig. 2. It can be clearly seen that the parameter η modifies the shape of the potential significantly. If $\eta = 0$ we obtain the sine-Gordon potential with the spatial period 4π. For the small values of

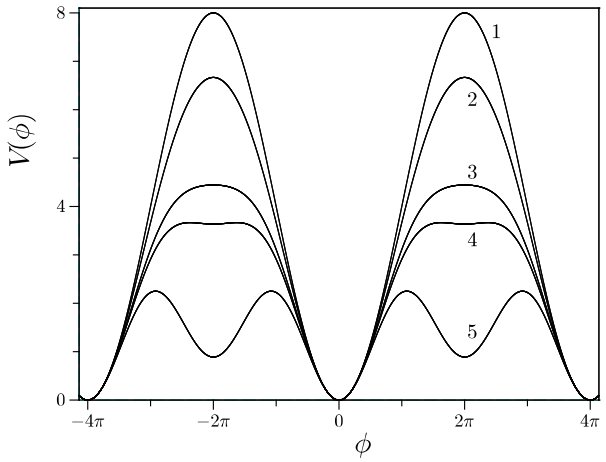

FIG. 2: Potential Eq. (4) for the different values of the anisotropy parameter: $\eta = 0$ (curve 1), $\eta = 0.1$ (curve 2), $\eta = 0.4$ (curve 3), $\eta = 0.6$ (curve 4) and $\eta = 4$ (curve 5).

η the potential barrier lowers, and if $\eta > 1/2$ a new local minimum appears at $\phi = 2(2n+1)\pi$, $n \in \mathbb{Z}$. In the limit $\eta \to \infty$ again the sine-Gordon potential is obtained, however, now its period is 2π.

The plane waves (Josephson plasmons) can be obtained via linearization of the equation of motion around the minima of the potential (4). The obtained dispersion laws read

$$\omega_0(q) = \sqrt{1 + 4\kappa \, \sin^2\frac{q}{2}} , \tag{5}$$

$$\omega_\pi(q) = \sqrt{\frac{2\eta - 1}{2\eta + 1} + 4\kappa \, \sin^2\frac{q}{2}} . \tag{6}$$

The first dispersion law corresponds to the small oscillations around the global minimum, while the second law

makes sense only if $\eta > 1/2$ and corresponds to the small oscillations around the metastable state. Due to finiteness of the array, the wavenumber $q \in [0, 2\pi)$ attains only discrete set of values $q_m = 2\pi m/N$, $m = \pm 1, \ldots, \pm N$. Note that the dispersion law (5) does not depend on the asymmetry parameter η.

A. The continuum limit

If $\kappa \gg 1$ the continuum limit can be applied and Eq. (1) reduces to the double sine-Gordon equation

$$\phi_{tt} - \phi_{xx} + \frac{2}{1+2\eta}\left(\eta \sin\phi + \sin\frac{\phi}{2}\right) + \alpha\phi_t = \gamma \ , \quad (7)$$

where the subscripts $_t$ and $_x$ correspond to the time and space derivatives, respectively. This equation has a large number of applications [21, 22], including the long Josephson junctions with the second harmonic in the current-phase relation [23].

The double sine-Gordon equation has topological soliton solutions that connect two adjacent global minima ($\phi = 0$ and $\phi = 4\pi$) and in the Hamiltonian limit $\alpha = \gamma = 0$ this solution reads [19, 21, 22]

$$\phi(x,t) = 2\pi + 4\arctan\left[\frac{1}{\sqrt{1+2\eta}}\sinh\left(\frac{x-vt}{\sqrt{1-v^2}}\right)\right] . \quad (8)$$

If $\eta = 1/2$ the soliton solution experiences an inflexion point in its center and for the large values of η the two 2π kinks that constitute the solution (8) become well separated.

B. Radiationless motion of discrete solitons. Sliding velocities

The dynamics of topological solitary waves in the lattices of the class, described by the Hamiltonian (3) (often referred to as the nonlinear Klein-Gordon lattices) has been well studied (see the reviews [24, 25] and the references therein). The main difference in the kink dynamics between the continuous Klein-Gordon model and its discrete counterparts is the following fact: the discreteness significantly obstructs the free soliton propagation, which is generic for the continuous models. If one looks for the *travelling-wave* solution of the form $\phi_n(t) = \phi(n - vt) \equiv \phi(z)$ that satisfies the differential-difference equation with the delay and advance terms

$$v^2\phi''(z) - \kappa\left[\phi(z+1) + \phi(z-1) - 2\phi(z)\right] - V'[\phi(z)] = 0, \quad (9)$$

he finds normally kinks that form a coupled state with the small-amplitude wave and that state travels with the same velocity v. In the continuum Klein-Gordon models the domain of admissible kink velocities is the interval $|v| < 1$. Thus, kinks in these continuum models form an one-parametric family of solutions with the kink velocity v being this parameter.

A detailed analytical [7, 8, 14–16] and numerical [7, 9–11] analysis shows that in a general case of the discrete Klein-Gordon model, the continuous family of moving kinks is reduced to the discrete finite set of *monotonic* ($\lim_{|n|\to\infty}\phi_n \to const$) travelling kink solutions with the velocities $v = \{v_0 \equiv 0, v_1, v_2 \ldots, v_k\}$. Further on, all velocities that satisfy $v_n \neq 0$ will be called *sliding* velocities since the kink slides along the lattice with these velocities without any radiation. These solutions can be called *discrete embedded solitons*. In the DSG equation there is only non-mobile ($v_0 = 0$) monotonic kink and there is no sliding velocities. In general, everywhere away from the sliding velocities, i.e., if $v \neq v_n$, the moving kinks are non-monotonic, have oscillating asymptotic tails and are often referred to as *nanopterons*. The monotonic solutions are of big importance since their energy is finite.

Using the so-called *pseudospectral* method, developed in [26–28], it is possible to compute the solution of Eq. (9) with the arbitrary desired numerical precision. In order to compute the *monotonic* solitary wave one has to monitor the tail of the solution $\phi(z)$ and change the velocity v until the amplitude of the oscillating tail becomes smaller than the defined tolerance value. We have done that for the DDbSG equation and in Fig. 3 we show the dependence of the first sliding velocity, v_1, on

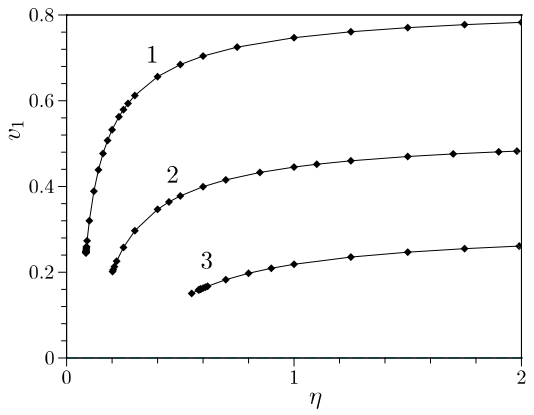

FIG. 3: Sliding velocities as a function of η for $\kappa = 1$ (curve 1), $\kappa = 0.5$ (curve 2) and $\kappa = 0.25$ (curve 3). The solid lines are used as a guide for an eye.

the asymmetry parameter η for the different values of the discreteness parameter κ. For these sets of parameters the spectrum of sliding velocities consisted of only one velocity, v_1. It appears that even for the rather small values of η (even $\eta \ll 1$, provided $\kappa \gtrsim 1$) there exists at least one sliding velocity. The value of the sliding velocity is smaller for the smaller values of the coupling parameter, and, it is interesting that the monotonic moving kinks can exist even in the strongly discrete lattice with $\kappa = 0.25$. The dependence $v_1(\eta)$ starts from some criti-

cal value of η, below this value the system does not allow for the sliding velocities, this is in agreement with the general theory of [11]. In the quasicontinuum approximation of DSG [18] or DDbSG [19], when the discrete Laplacian is approximated up to ϕ_{xxxx}, the moving kink exists again only for the selected set of sliding velocities, but these velocities (depending on the model parameters) can be arbitrarily small.

The substitution of the solution of Eq. (9) with the sliding velocity v_1 into the actual DDbSG equation (1) results in the kink propagation continuously with this velocity v_1 without any noticeable radiation. The following numerical experiment demonstrated this. The moving kink obtained as a solution of Eq. (9) with the sliding velocity v_1 has been launched with the velocity v_*, that may differ from v_1. The evolution of the soliton center of mass is shown in Fig. 4. It appears that if the initial

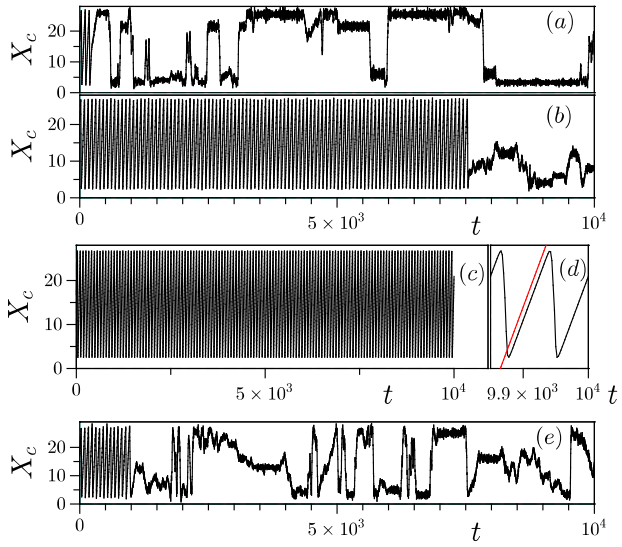

FIG. 4: (Color online) Kink center of mass evolution in the Hamiltonian limit for $\kappa = 0.5$, $\eta = 0.6$, $v_1 = 0.399493$ with the initial boost velocity $v_* = 0.97v_1$ (a), $v_* = 0.99v_1$ (b), $v_* = v_1$ (c,d) and $v_* = 1.25v_1$ (e). The red line in the panel (d) corresponds to the center of mass moving with the sliding velocity $X(t) \sim v_1 t$.

soliton velocity differs from v_1 insignificantly the soliton can travel for a long time around the lattice [see Fig. 4(b)]. Otherwise it gets pinned rather fast as shown in Figs. 4(a,e). If $v_* = v_1$ the soliton travels without any significant slowing down or radiation [see the panels (c) and (d)].

IV. THE CURRENT-VOLTAGE CHARACTERISTICS

Now we can start constructing the current-voltage characteristics (CVCs) for the non-zero values of bias and dissipation.

A. The continuum limit

In the continuum limit one can use the power balance method from Ref. [29] and compute the equilibrium fluxon velocity. The power balance equation reads $\bar{V}_c\gamma = 4\pi\sqrt{\kappa}\ v\gamma/N = -P_{diss}$. Here $\bar{V}_c$ is the average voltage drop, produced by the fluxon moving with the velocity v. If we assume that the perturbation, caused by the bias and dissipation, is small and the fluxon shape is given by the exact solution of the unperturbed continuous equation (7), we can compute the power of the dissipative losses

$$P_{diss} = -\alpha\int_{-\infty}^{+\infty}\phi_t^2 dx = -\frac{16\alpha v^2}{\sqrt{1-v^2}}\Phi(\eta)\ , \quad (10)$$
$$\Phi(\eta) = 1 + \frac{1}{\sqrt{2\eta(2\eta+1)}}\ \mathrm{arctanh}\sqrt{\frac{2\eta}{1+2\eta}},$$

where the solution (8) has been substituted in the above integral. From this equation one can find the equilibrium fluxon velocity v and the average voltage drop

$$\bar{V}_c = \sqrt{\kappa}\frac{4\pi v_\infty}{N} = \sqrt{\kappa}\frac{4\pi}{N}\left[1+\Phi^2(\eta)\left(\frac{4\alpha}{\pi\gamma}\right)^2\right]^{-1/2}\ . \quad (11)$$

The auxiliary function $\Phi(\eta)$ attains two important limits: $\lim_{\eta\to 0}\Phi(\eta) = 2$ and $\lim_{\eta\to\infty}\Phi(\eta) = 1$. In both these limits the well-known formula for the SG equation [29] is restored. Since $\Phi(\eta) > 1$ for any finite positive η, the slope of the CVC near the origin ($\gamma \ll 1$) will be more and more flat as η increases: $\bar{V}_c \simeq \sqrt{\kappa}\pi^2\gamma/[N\alpha\Phi(\eta)]$.

B. The numerical results

The numerically-computed CVCs are shown in Figs. 5-6 by the markers while the blue solid lines correspond to the analytical formula (11) that stems from the continuum approximation. This approximation predicts the continuous curve $\gamma = \gamma(\bar{V})$ and appears to work well only for the small values of γ. Surprisingly, it gives the correct slope of the CVC near the origin even for the strongly discrete array ($\kappa = 0.5$), however it works rather poorly for the larger values of the external bias.

The numerically computed average voltage drop is defined as

$$\bar{V} = \frac{1}{N}\sum_{n=1}^{N}\lim_{t\to\infty}\frac{1}{t}\int_0^t \dot{\phi}_n(t')dt'\ . \quad (12)$$

If the fluxon propagates with the constant velocity v it produces the average voltage drop $\bar{V} = 4\pi v/N$. The CVC calculation procedure can be described as follows. We start at the zero bias ($\gamma = 0$) and integrate the equations of motion (1) with the 4th order Runge-Kutta method for each value of γ during the time $t > 10\alpha^{-1}$.

When the average voltage (12) reaches the desirable tolerance, γ is increased by some small amount and the procedure is repeated again. The same calculation has been performed when γ is decreased till $\gamma = 0$. Since the CVCs demonstrate complex hysteretic structure (sometimes multiple), each branch has been path-followed back and forth between its respective ends.

The typical CVCs consists of the cascades of separate branches that appear due to the fluxon coupling with the plasmon modes, see theoretical [1, 30–32] and experimental papers [1, 32–34]. While moving along the array, the fluxon excites the plasmon modes and forms a bound state that propagates with the same velocity. If v is the fluxon velocity, the plasmon phase velocity should equal v as well. Thus, the plasmon wavenumber is given by the root of the following equation:

$$\omega_0(q) - vq = 0 \ , \tag{13}$$

where $\omega_0(q)$ is the plasmon dispersion law (5). Due to periodicity of the boundary conditions the phase locking in the array would occur if the finite number of the Josephson phase oscillations will fit into one cycle of the fluxon journey along the array. In other terms this means that a certain number of the plasmon wavelength should be fitted in the array, as one can easily see from the inset in Fig.5(a), where the $\dot{\phi}_n$ distribution is given from the two neighbouring voltage steps. Thus, the different number of oscillations fitted in the array corresponds to the different branch of the CVC. This situation has been reported in the literature [1, 30] together with the approximate values of the voltage steps, so we will not dwell on it any longer.

1. *Signatures of the sliding velocities*

Analysis of these CVCs shows that there exist both qualitative and quantitative differences between the cases when the DDbSG equation has at least one sliding velocity in the Hamiltonian limit and when there is no such a velocity. These differences can be summarized in the following two paragraphs.

a. **The inaccessible interval (gap) within the range of admissible voltages.** It appears that if η is too small, the underlying Hamiltonian problem does not possess a sliding velocity, we face the situation when the CVC consists of the branches shown in of Fig. 5(a), and the interval between these branches along the $\bar{V}$ axis decreases as $\bar{V}$ decreases. The same is true about the length of these branches in the γ direction. A small gap between the voltage steps can be noticed in the interval $0.06 \lesssim \bar{V} \lesssim 0.07$. This interval corresponds to the situation when the number of roots of Eq. (13) has changed from one to three. The kind of picture described in Fig. 5(a) is the same as observed in the simple driven and damped DSG equation [30].

Yet a different situation occurs if in the Hamiltonian limit there is at least one sliding velocity. According to the results of Subsec. III B for $\kappa = 0.5$ there should be a sliding velocity if $\eta > 0.202$, thus, this is the case for the CVCs in the panels (b)-(d). In these figures one can easily spot a significant *inaccessible voltage interval* (IVI) or a gap, i.e., there is an forbidden interval in $\bar{V} \in [V^-_{IVI}, V^+_{IVI}]$ where no voltage can be produced by the moving fluxon. This interval is not noticeable for $\eta = 0.3$, $\alpha = 0.05$ [see Fig. 5(b)], but is clearly seen for $\alpha = 0.02$. However, the IVI increases strongly as η increases [see Figs. 5(c,d)]. It is important to remark that the upper edge of this inaccessible interval, V^+_{IVI}, moves closer and closer towards the voltage $4\pi v_1/N$, produced the fluxon moving with the sliding velocity v_1.

b. **The IVI increases as the damping parameter decreases.** Another important observation is that as the dissipation decreases, the width of the IVI increases. The two sets of data are plotted in Figs. 5(b-c), for $\alpha = 0.05$ and $\alpha = 0.02$. In addition, in Fig. 5(d) the data for $\alpha = 0.01$ are given. One can notice that the IVI becomes quite pronounced for $\eta = 0.3$ if the damping coefficient is reduced from $\alpha = 0.05$ to $\alpha = 0.02$. This is seen even better in Figs. 5(c,d) where the IVI is well defined for $\alpha = 0.05$ and its width increases with the growth of η and with the decreasing of α. In particular, we note that there are fewer branches for $\bar{V}$ below the IVI ($\bar{V} < V^-_{IVI}$) if α is decreased. The length of these branches along the γ axis decreases as well, compare, for example, the data in Fig. 5(d), where only one branch below the IVI survives if the dissipation parameter is reduced from $\alpha = 0.05$ to $\alpha = 0.02$. If α is reduced further till $\alpha = 0.01$ there is no other CVC branches below the IVI, i.e., $V^-_{IVI} = 0$. The two CVCs for the smaller value of the discreteness constant ($\kappa = 0.25$) for $\eta = 0.3$ (no sliding velocity) and $\eta = 0.6$ (one sliding velocity $v_1 = 0.162871$) are given in Fig. 6. Here the IVI is clearly seen for $\eta = 0.6$ and the behaviour of its edges is the same as in Fig. 5: $V^+_{IVI} \to 4\pi v_1/N$ as $\alpha \to 0$ (see the inset) while $V^-_{IVI} = 0$.

The upper edge of the IVI, V^+_{IVI} is positioned close to the value $4\pi v_1/N$, where v_1 is the respective sliding velocity. By defining the detuning parameter

$$\nu = \left| V^+_{IVI} - \frac{4\pi}{N} v_1 \right| \ , \tag{14}$$

and presenting it in Tab. I, we demonstrate that the IVI is directly associated with the sliding velocity of the DDbSG equation in the Hamiltonian limit. Indeed, the

$\alpha\backslash\eta$	0.6	1	1.5
0.05	0.0075	0.0017	0.0013
0.02	0.0070	0.0014	0.0013
0.01	0.0050	0.0014	0.0012
0.005	0.0041	0.0010	0.0011

TABLE I: The detuning parameter ν [see Eq. (14)] for $\kappa = 0.5$ as a function of α and η.

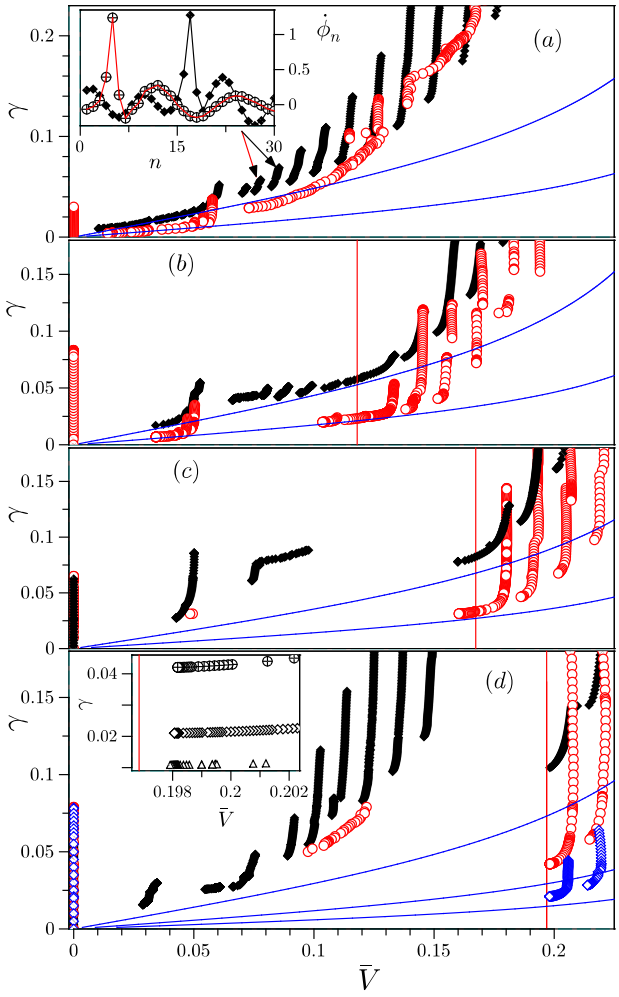

FIG. 5: (Color online) Current-voltage curves for $\kappa = 0.5$, $N = 30$, $\alpha = 0.05$ (black ♦), $\alpha = 0.02$ (red ○), $\alpha = 0.01$ (blue ◇) and $\eta = 0.1$ (a), $\eta = 0.3$ (b), $\eta = 0.6$ (c) and $\eta = 1.5$ (d). The blue solid lines correspond to the respective CVC in the continuum limit, Eq. (13). The red vertical lines in (b)-(d) are given by $4\pi v_1/N$, where v_1 is the sliding velocity for the respective value of η (see Fig. 3). The inset in the panel (a) shows the distribution of $\dot{\phi}_n$ that correspond to the branches of the CVC pointed by the arrows at $\alpha = 0.05$. The distribution corresponding to the branch on the right is given by ♦ while ⊕ corresponds to the branch on the left. The inset in the panel (d) shows the details of CVCs in the neighbourhood of the sliding velocity for $\alpha = 0.02$ (⊕), $\alpha = 0.01$ (◇) and $\alpha = 0.005$ (Δ).

detuning parameter decreases as η increases as well as $\alpha \to 0$.

These results can have the following mathematical interpretation. If the Hamiltonian system possesses a sliding velocity v, even the small perturbation by adding non-zero α and γ creates an attractor that corresponds to the fluxon motion with the velocity close to v (see Ref. [35]). Thus, for small α we observe that as $\gamma \to 0$, the fluxon moves with the velocity close to v. If there

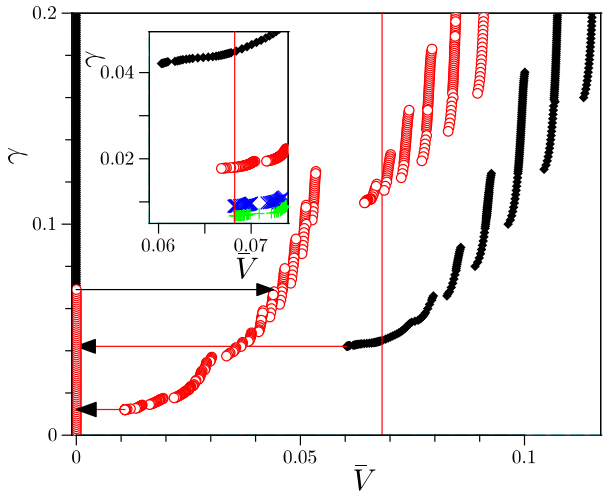

FIG. 6: (Color online) Current-voltage curves for $\kappa = 0.25$, $\alpha = 0.05$, $\eta = 0.6$ (black ♦) and $\eta = 0.3$ (red ○). The inset shows the details of CVCs in the neighbourhood of the sliding velocity for $\eta = 0.6$, $\alpha = 0.05$ (black ♦), $\alpha = 0.02$ (red ○) $\alpha = 0.01$ (blue ×) and $\alpha = 0.0075$ (green +). The red vertical line marks the voltage drop that corresponds to the respective sliding velocity in the Hamiltonian limit.

is no sliding velocity, for the same values of α and γ the fluxon either moves with very small velocity close to 0, or is simply pinned due to discreteness. This situation is well seen in Figs. 5(a) and 6, where the CVC approaches close to the origin but never attains it.

2. *Chaotic vs. regular regimes of motion*

Observation of the branches of on the CVCs in Figs. 5-6 reveals that the most of these branches are almost vertical lines. Only at their bottom ends these branches become bent towards the lower voltages. The branches near the IVI are almost horizontal with small vertical parts. This transition goes on smoothly as γ decreases. However, there are some isolated branches that fall out from the usual picture. For example, in Fig. 5(c) there is a branch just below the IVI, with the weakly tilted top part and almost vertical bottom part. Also, in Fig. 5(d) at $\alpha = 0.02$ there is an isolated and significantly tilted branch just below the IVI. Hence, one should focus on the nature of the dynamics that fluxon undergoes when traversing the array. In order to solve this question, the largest Lyapunov exponent (LLE) λ has been computed (with the help of the Benettin algorithm [36]) for the three branches of the CVC from Fig. 5(c) at $\alpha = 0.05$. We have taken the closest branches to the IVI, one above it, with voltages changing in the range $0.16 \lesssim \bar{V} \lesssim 0.18$, and two below it, with the voltages in the range $0.074 \lesssim \bar{V} \lesssim 0.1$ and $0.043 \lesssim \bar{V} \lesssim 0.05$.

The respective dependencies $\lambda(\gamma)$ are given by the lines 1 (black), 2 (blue) and 3 (red) in Fig. 7(a). We observe that $\lambda = 0$ for the line 1 (black), and this line corresponds to the branch of the CVC that is just above the IVI. For the non-bounded trajectories in the autonomous system there is always a zero Lyapunov exponent, thus the dynamics on this branch is regular. In the curve 2 (blue) LLE is positive in the interval $0.077 \lesssim \gamma \lesssim 0.088$ that corresponds approximately to the top part of the branch and becomes zero in the interval $0.062 \lesssim \gamma \lesssim 0.077$ that corresponds approximately to the bottom part of the branch. From the respective CVC [Fig. 5(c)] one can determine that the dynamics is chaotic when the branch is strongly tilted and is regular when the CVC is almost vertical. Finally, the dependence 3 for the lowest (closest to the origin) branch shows that dynamics is regular at the upper part of the branch and becomes chaotic as γ decreases. Several switchings from chaotic to regular motion and back can be observed as well.

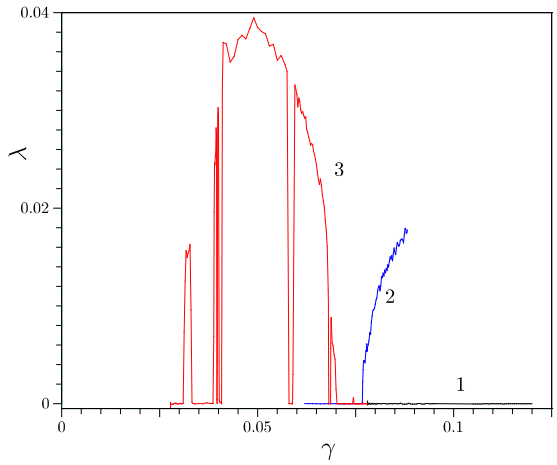

FIG. 7: (Color online) Largest Lyapunov exponent as a function of bias for three branches of the CVC, given in Fig. 5(c). The parameters are: $\kappa = 0.5$, $\alpha = 0.05$ and $\eta = 0.6$. Different lines correspond to the different branches of the CVC. See text for details.

The power spectrum of $\dot{\phi}_{N/2}$, defined as

$$I(\Omega) = \left| \int_{-\infty}^{+\infty} \dot{\phi}_{N/2}(t) e^{-i\Omega t} dt \right|^2 , \qquad (15)$$

is plotted in Fig. 8. It has been computed for the several values of γ at the CVC branches, discussed in the previous paragraph. First we consider the branch above the IVI ($\bar{V} > V^+_{IVI}$), for which the LLE is always zero (line 1 in Fig. 7). As one can see in Fig. 8(a), the spectrum consists of the equidistant peaks, positioned at $\Omega = n\bar{V}/2$, $n = 1, 2, \ldots$. Thus, the trajectory is the limit cycle with the frequency $\bar{V}/2$. This means that the fluxon reconstructs its shape completely after travelling around the array twice. The respective position on the CVC [see Fig. 5(c)] corresponds to $\gamma = 0.11$, $\bar{V} = 0.1789$.

Next we turn our attention to the second branch of the CVC, that lies just below the IVI. On the weakly tilted part of the branch ($\gamma = 0.08$) the dynamics is chaotic, as has been seen from the LLE dependence (line 2 in Fig. 7). The power spectrum consists of the wideband [see Fig. 7(b)] and several peaks at $\Omega \sim \bar{V}/2, \bar{V}, 3\bar{V}/2$. The average voltage drop here is $\bar{V} = 0.0825$. Another point on the same branch corresponds to the vertical part of it ($\gamma = 0.075$). Dynamics there is regular, the peaks [see the panel (c)] at $\Omega = n\bar{V}/2$, $n = 1, 2, \ldots$ can be easily spotted in the low-frequency region. There are other peaks, associated with some frequency that is significantly lower than $\bar{V}$. Hence, the respective trajectory is quasiperiodic. Finally, on the closest to the origin branch of the CVC at $\gamma = 0.045$ chaotic dynamics has been observed (see line 3 of Fig. 7). This is confirmed further by the broadband power spectrum, shown in Fig. 8(d). However, the peaks at $\Omega = n\bar{V}/2$, $n = 1, 2, \ldots$ can be spotted much better comparing to another chaotic case, shown in the panel (b). We have also checked the dynamics of the isolated branch in Fig. 5(d) at $\alpha = 0.02$. Both the LLE calculations and the spectral analysis show that the dynamics there is also chaotic and the power spectrum is similar to the spectrum in Fig. 8(b).

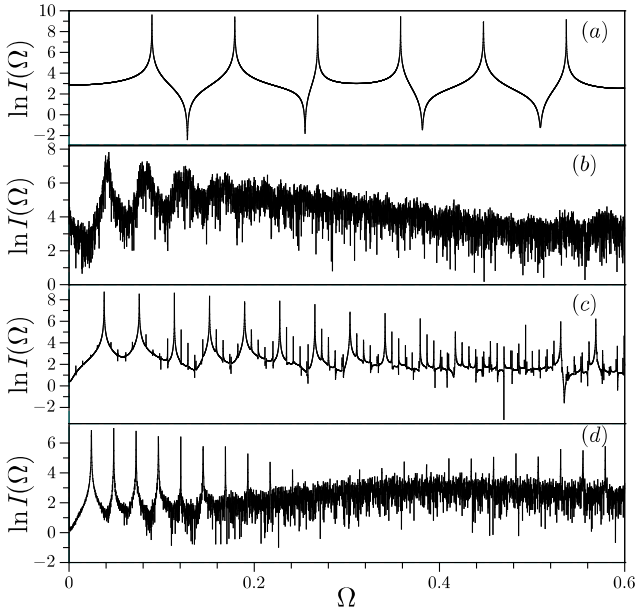

FIG. 8: Power spectra of the $\dot{\phi}_{N/2}$ variable for the different values of bias at (a) $\gamma = 0.11$, $\bar{V} = 0.1789$; (b) $\gamma = 0.08$, $\bar{V} = 0.08241$; (c) $\gamma = 0.075$, $\bar{V} = 0.07585$; (d) $\gamma = 0.045$, $\bar{V} = 0.04825$.

3. The critical depinning current

The careful investigation of the CVCs demonstrates the non-monotonic dependence of the critical depinning current γ_c on the asymmetry parameter η. The critical depinning current is the minimal bias current which can sustain the pinned fluxon state ($\bar{V} = 0$ on the CVC). Indeed, as on can see from Fig. 6, the critical depinning current equals $\gamma_c = 0.0695$ for $\eta = 0.3$ and $\gamma_c = 0.267$ for $\eta = 0.6$. At first glance this seems to be surprising, as we can naively suppose that the pinning of the fluxon is defined by the barrier height of the double sine-Gordon potential $V(\phi)$ (4). This suggestion is obviously wrong, since the height of $V(\phi)$ decreases with the growth of η. Moreover, the dependence of the critical current γ_c on the asymmetry parameter η appears to be non-monotonic, as shown in Fig. 9. In order explain this behaviour it is useful to compute the PN potential and its barrier as a function of η. The concept of the PN potential is known for a long time [24] and is used to describe the motion a topological soliton in the discrete media as a motion of an inertial particle in the field produced by the spatially periodic potential. This is, in fact, the PN potential, $V_{PN}(X) = V_{PN}(X+1)$ and X is the soliton center of mass. The PN barrier is defined as $\Delta E_{PN} = \max_X[V_{PN}(X)] - \min_X[V_{PN}(X)]$. If $\kappa \gg 1$ the PN potential can be computed analytically[37] and for the DSG equation it satisfies $V_{PN}(X) \propto 1 - \cos X$. In our case the perturbational approach will fail, therefore the PN potential has to be computed numerically.

In Fig. 9 the PN barrier as a function of the asymmetry parameter η is demonstrated by the solid black line. The dependence is non-monotonic and has a clear minimum for the same η where the $\gamma_c(\eta)$ has a minimum. At this minimum the barrier is decreased by the order of magnitude. This non-monotonic behaviour of the PN barrier as a function of the shape parameter (and also of the coupling constant κ) is already known for other discrete Klein-Gordon systems [9, 10, 38] with the on-site potentials that depend on the shape parameter. The reason is the following. Under the certain set of parameters ΔE_{PN} both the site-centered and bond-centered static kink states are the local minima of the total energy, while the local maximum corresponds to the asymmetric configuration, which is intermediate between the site-centered and bond-centered states. For these parameters the function ΔE_{PN} attains its minimum. It is important to note that if $\eta = 0$, i.e., in the case of the conventional DSG equation, the bond-centered state is always a local minimum and the site-centered state is always a saddle point. Thus, for the DSG equation ΔE_{PN} is simply the difference of the energies of these kink configurations. The inset of Fig. 9 shows the pinned fluxon profiles for $\eta = 0.26$ and $\eta = 0.31$, while the $\gamma_c(\eta)$ dependence attains its minimum at $\eta \approx 0.28$. In the former case the bond-centered fluxon is the local minimum of the energy while in the latter case it is the site-centered fluxon. The fluxon profiles look a bit asymmetric because the non-zero bias makes the total potential energy asymmetric with respect to the point $\phi = 0$.

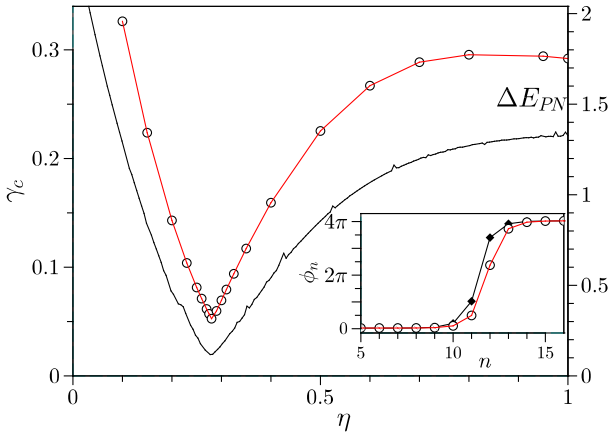

FIG. 9: (Color online). Critical depinning current (∘, left scale) and the PN barrier (solid black line, right scale) as a function of the asymmetry parameter η for $\kappa = 0.25$. The red line is used as a guide for an eye. The inset shows the distribution of the ϕ_n for the pinned fluxon at $\eta = 0.26$, $\gamma = 0.07111$ (♦) and $\eta = 0.31$, $\gamma = 0.079$ (∘). The solid lines are used as guides for an eye.

V. DISCUSSION AND CONCLUSIONS

In this article it has been demonstrated how the features of the kink mobility in the discrete Klein-Gordon models can be manifested in realistic systems. As a particular system the array of the asymmetric three-junction SQUIDs has been considered. This object is described by the discrete double sine-Gordon equation (DDbSG).

The main result can be summarized as follows. In the Hamiltonian limit the DDbSG equation alongside with other similar models, like the Peyrard-Remoissenet [38] and the double Morse [10] chains, allows for a discrete set of kink velocities (*sliding* velocities) with which monotonic ($\lim_{|n|\to\infty} \phi_n \to const$) kinks can propagate. These excitations belong to the family of the so-called *embedded* solitons [17, 18]. The signature of the sliding velocities can be spotted on the CVCs of the array. This signature is a significant inaccessible voltage interval (IVI), i.e. the voltage that cannot be produced by the moving fluxon. As the voltage drop is proportional to the fluxon velocity, one can speak also about the inaccessible velocity interval. This interval does not appear if the asymmetry parameter $\eta = I_c^{(r)}/I_c^{(l)}$ is too small and there is no sliding soliton velocities in the Hamiltonian limit. The IVI becomes more pronounced if η increases or if $\alpha \to 0$. In particular, the lower edge of the IVI tends to zero, while the upper edge converges to the value $4\pi v/N$ with v being the sliding velocity.

Another important result is the significant lowering of the critical pinning current due to the change of η. The explanation is based on the non-trivial dependence of the PN barrier on the asymmetry parameter. Similar results on the lowering of the activation barrier for solitons have been reported earlier for other lattice models [21, 38, 39].

It is also important to comment on the connection with the problem of the radiationless motion of the bunched kink (fluxon) states in the ordinary DSG lattice. The symmetric SQUID array, or, equivalently the array of parallel shunted small Josephson junctions [40] is described by the DSG equation. It has been shown in several cases both theoretically [9, 11, 40, 41] and experimentally [42] that the radiationless sliding of the coupled pair of several kinks (4π, 6π, etc.) is possible for the selected set of kink velocities. This phenomenon has been treated analytically in the quasi-continuum approximation in Refs. [18, 19], but it takes place even in the sufficiently discrete array ($\kappa < 1$) as well. In the limit $\eta \to \infty$ the double sine-Gordon potential in (4) becomes the ordinary sine-Gordon potential with the period 2π, thus, the above-mentioned result of the bound state of two 2π kinks is the special case of the kink mobility of the DDbSG equation in the limit $\eta \to \infty$.

In the current model the role of the mutual inductances of the array cells has been neglected in accordance the previous work [20]. If the mutual inductances are taken into account, the dynamics of the Josephson phases should be described not by the DDbSG equation (1) but by Eq. (1) of Ref. [20]. The main difference between these two equations lies in the nature of the coupling term. While in Eq. (1) there is coupling only between the nearest neighbouring Josephson phases, the case with mutual inductances accounts for coupling of all Josephson phases of the array. The existence of the sliding velocities depends primarily on the properties of the current-phase relation that contains the $\sin\phi_n$ and the $\sin(\phi_n/2)$ terms, and not on the interaction. Therefore, we do not expect any qualitative differences if the mutual inductances are taken into account. The quantitative differences may occur because the value of the sliding velocity depends of the coupling parameter.

Finally, we remark that the DDbSG equation (1) can describe another system - the parallel array of Josephson junctions that have the biharmonic current-phase relation $I_c(\phi) = I_{c,1}\sin\phi + I_{c,2}\sin 2\phi$ [43] [here the substitution $\phi \to \phi/2$ should be performed in order to get Eq. (1)]. This, in particular, is true for the superconductor-ferromagnet-superconductor (SFS) and superconductor-ferromagnet-insulator-superconductor (SFIS) junctions. Naturally, the phenomena, discussed in this paper apply to the arrays of the SFS and SFIS junctions as well.

Acknowledgements

One of the authors (Y.Z.) acknowledges the financial support from the Ukrainian State Grant for Fundamental Research No. 0112U000056.

[1] S. Watanabe, H. S. J. van der Zant, S. H. Strogatz, and T. P. Orlando, Physica D **97**, 429 (1996).
[2] A. V. Ustinov, Physica D **123**, 315 (1998).
[3] A. Fedorov, A. Shnirman, G. Schon and A. Kidiyarova-Shevchenko, Phys. Rev. B **75**, 224504 (2007).
[4] D. V. Averin, K. Rabenstein, and V. K. Semenov, Phys. Rev. B **73**, 094504 (2006).
[5] N. Lazarides and G. P. Tsironis, Superconductor Science Technology **26**, 084006 (2013).
[6] M. Nishida, T. Kanayama, T. Nakajo, T. Fujii, and N. Hatakenaka, Physica C **470**, 832 (2010).
[7] S. Flach, Y. Zolotaryuk, and K. Kladko, Phys. Rev. E **59**, 6105 (1999).
[8] V. H. Schmidt, Phys. Rev. B **20**, 4397 (1979).
[9] A. V. Savin, Y. Zolotaryuk, and J. C. Eilbeck, Physica D **138**, 265 (2000).
[10] V. M. Karpan, Y. Zolotaryuk, P. L. Christiansen, and A. V. Zolotaryuk, Phys. Rev. E **66**, 066603 (2002).
[11] A. Aigner, A. Champneys, and V. Rothos, Physica D **186**, 148 (2003).
[12] Y. Zolotaryuk, J. C. Eilbeck, and A. V. Savin, Physica D **108**, 81 (1997).
[13] I. V. Barashenkov, O. F. Oxtoby, and D. E. Pelinovsky, Phys. Rev. E **72**, 035602(R) (2005).
[14] O. Oxtoby, D. E. Pelinovsky, and I. V. Barashenkov, Nonlinearity **19**, 217 (2006).
[15] G. L. Alfimov, E. V. Medvedeva, and D. E. Pelinovsky, Phys. Rev. Lett. **112**, 054103 (2014).
[16] S. V. Dmitriev, A. Khare, P. G. Kevrekidis, A. Saxena, and L. Hadzievski, Phys. Rev. E **77**, 056603 (2008).
[17] A. Champneys, B. Malomed, J. Yang, and D. Kaup, Physica D **152-153**, 340 (2001).
[18] A. Champneys and Y. S. Kivshar, Phys. Rev. E **61**, 2551 (2000).
[19] M. M. Bogdan, A. Kosevich, and G. A. Maugin, Wave Motion **34**, 1 (2001).
[20] R. D. Bock, J. R. Phillips, H. S. J. van der Zant, and T. P. Orlando, Phys. Rev. B **49**, 10009 (1994).
[21] C. A. Condat, R. A. Guyer, and M. D. Miller, Phys. Rev. B **27**, 474 (1983).
[22] D. K. Campbell, M. Peyrard, and P. Sodano, Physica D **19**, 165 (1986).
[23] E. Goldobin, D. Koelle, R. Kleiner, and A. Buzdin, Phys. Rev. B **76**, 224523 (2007)
[24] O. M. Braun and Y. S. Kivshar, Phys. Rep. **306**, 2 (1998).
[25] L. M. Floria and J. J. Mazo, Adv. Phys. **45**, 505 (1996).
[26] D. Hochstrasser, F. Mertens, and H. Büttner, Physica D: Nonlinear Phenomena **35**, 259 (1989).
[27] J. C. Eilbeck and R. Flesch, Phys. Lett. A **149**, 200 (1990).
[28] D. Duncan, J. Eilbeck, H. Feddersen, and J. Wattis, Physica D **68**, 1 (1993).

[29] D. W. McLaughlin and A. C. Scott, Phys. Rev. A **18**, 1652 (1978).
[30] A. V. Ustinov, M. Cirillo, and B. A. Malomed, Phys. Rev. B **47**, 8357 (1993).
[31] O. M. Braun, B. Hu, and A. Zeltser, Phys. Rev. E **62**, 4235 (2000).
[32] H. S. J. van der Zant, T. P. Orlando, S. Watanabe, and S. H. Strogatz, Phys. Rev. Lett. **74**, 174 (1995).
[33] M. Cirillo *et al*, Phys. Lett. A, Phys. Lett. A **183**, 383 (1993).
[34] A. V. Ustinov *et al*, Phys. Rev. B **51**, 3081 (1995).
[35] P. G. Kevrekidis and Y. Zolotaryuk, *Differential-Difference Equations and their Depinning Transitions*, New Developments in Soliton Research (Nova Science Publishers, Inc., 2006).
[36] G. Benettin, L. Galgani, A. Giorgilli and J. M. Strelcyn, Meccanica **15**, 9 (1980).
[37] Y. Ishimori and T. Munakata, J. Phys. Soc. Japan **51**, 3367 (1982).
[38] M. Peyrard and M. Remoissenet, Phys. Rev. B **26**, 2886 (1982).
[39] A. V. Savin and A. V. Zolotaryuk, Phys. Rev. A **44**, 8167 (1991).
[40] A. V. Ustinov, B. A. Malomed, and S. Sakai, Phys. Rev. B **57**, 11 691 (1998).
[41] M. Peyrard and M. D. Kruskal, Physica D **14**, 88 (1984).
[42] J. Pfeiffer, M. Schuster, A. A. Abdumalikov, and A. V. Ustinov, Phys. Rev. Lett. **96**, 034103(4) (2006).
[43] A. A. Golubov, M. Y. Kupriyanov, and E. Ilichev, Rev. Mod. Phys. **76**, 411 (2004).